




Article

A Finite Element Analysis of Cold Deep Drawing of Al Alloy Considering Friction Condition and Corner Design of Plunger

Warda Bahanan ^{1,†}, Siti Fatimah ^{1,†} , Jae Hoon Go ¹, Jeong Moo Oh ¹, Min Jun Kim ², Myung Jae Kim ³, Jee-Hyun Kang ¹ , Dong-Ju Kim ^{2,*}, I Putu Widianara ^{1,*} and Young Gun Ko ^{1,*} 

¹ School of Materials Science and Engineering, Yeungnam University, Gyeongsan 38541, Republic of Korea

² SeA Mechanics Co., Ltd., Gumi 39379, Republic of Korea

³ Jaeyoung Tech., Gimcheon 39536, Republic of Korea

* Correspondence: jks4721@seamechanics.com (D.-J.K.); iputuwidiantara89@yu.ac.kr (I.P.W.);
younggun@ynu.ac.kr (Y.G.K.)

† These authors contributed equally to this work.

Abstract: This study presents an innovative methodology that integrates experimental investigations with finite element simulations to ascertain the validity and reliability of Al 3104 sheet metals during cold deep drawing. Focusing on the nose plunger radius and coefficient of friction at a fixed speed and temperature (25 °C), five different scenarios are utilized to simulate the optimum parameters. Through a detailed strain history analysis from simulations, the initiation of bending in the corner is precisely identified, with a validation achieved through a strain analysis obtained via digital image correlation. The study delves into the influence of strain and strain rate on the microstructures and mechanical properties near the corner region. It highlights the superior efficacy of strain-based criteria in characterizing deformation behavior. Notably, the strain distributions during the onset of bending and severe bending align remarkably well with the established simulation data. In brief, this work introduces an integrated approach that harmoniously combines computational simulations with empirical observations, resulting in significant ramifications for precisely comprehending and forecasting the strain distribution in metal forming operations.



Citation: Bahanan, W.; Fatimah, S.; Go, J.H.; Oh, J.M.; Kim, M.J.; Kim, M.J.; Kang, J.-H.; Kim, D.-J.; Widianara, I.P.; Ko, Y.G. A Finite Element Analysis of Cold Deep Drawing of Al Alloy Considering Friction Condition and Corner Design of Plunger. *Lubricants* **2023**, *11*, 388. <https://doi.org/10.3390/lubricants11090388>

Received: 28 August 2023

Revised: 5 September 2023

Accepted: 8 September 2023

Published: 10 September 2023



Copyright: © 2023 by the authors. Licensee MDPI, Basel, Switzerland. This article is an open access article distributed under the terms and conditions of the Creative Commons Attribution (CC BY) license (<https://creativecommons.org/licenses/by/4.0/>).

Keywords: Al alloy; cold deep drawing; finite element analysis; plunger radius; friction coefficient

1. Introduction

The increasing demands for lightweight design in the transport industry have led to an extensive use of lightweight materials such as aluminum (Al) and its alloys [1]. The forming of Al sheets, however, presents significant challenges due to the low formability and the increased susceptibility to friction [1]. A particularly noteworthy subset of Al alloys is the 3xxx series, characterized by a fundamental Al-manganese composition [2]. With manganese as the primary alloying element, this series embodies a delicate balance of attributes: a good formability, a moderate strength, and an inherent resistance to corrosion [2]. As a result, the 3xxx series alloys would be particularly favored for applications that demand complex geometries featuring gentle curves and nuanced bends. Moreover, the series 3xxx, when subjected to H32 tempering, exhibit a balance between strength and formability, which is favorable in the realm of deep drawing applications [3,4]. The H32 heat treatment is a controlled cooling process designed to offer several benefits in terms of improving formability and reducing the anisotropy, the directional variation in mechanical properties. The reduced anisotropy ensures that the material flows more evenly during the forming process, resulting in smoother and more uniform surfaces on the finished parts [5].

The process of deep drawing stands as a cornerstone of contemporary manufacturing, enabling the transformation of flat sheet metal into three-dimensional structures that underpin a diverse application of products across industries [6]. In the realm of current

manufacturing, the deep drawing process holds a substantial importance due to its significant contributions to production capacity, energy efficiency, and the potential for enhancing processes [7,8]. During the deep drawing process, a variety of factors might contribute to product failure [7,8]. This failure typically manifests as wrinkling, tearing, earing, and rupture [7,8]. These studies contained descriptions of material properties, die design, and operating factors such as blank holder load, friction coefficients, deep drawing ratio, and maximum drawing force; a careful control of these parameters helps lower the likelihood of failure for drawing parts [9]. Singh et al. [10] discovered the effectiveness of deep drawing variables, including die shoulder radii, plunger nose radii, friction coefficients, and deep drawing ratios for cylinder-shaped parts.

The die radius is the largest contributing factor when compared to other processing parameters, including friction coefficient. In a similar study, Colgan and Monaghan [11] concluded that the geometry parameters were generally the most important influential factors in a deep drawing process, especially the die radius. They observed that smaller die radii restricted material draw in and increased the required plunger force, therefore promoting stretching rather than drawing, which may result in excess thinning. Another study conducted by Yusop and Abdullah [12] evaluated cup drawing simulations and concluded that optimum radii were necessary to reduce component thinning. Large corner radii can reduce sample thinning and thickening defects when they are compared to the smaller ones [13]. However, a lack of structure was identified when observing these trends and sensitivities in the literature. On the other hand, the friction coefficient was found to be the best parameter among die radii and blank holder force (BHF) to achieve a decent quality of the formed component [14].

The relationship between anisotropy and deep drawing lies in how the anisotropic properties of the sheet metal material can influence the deep drawing process. When deep drawing a sheet of anisotropic material, the orientation of the material relative to the direction of deformation can significantly affect the success of the process. When performing deep drawing on a sheet of metal with anisotropic properties, it is crucial to align the sheet's orientation in a way that optimizes its ductility and minimizes the likelihood of material failure, such as tearing or wrinkling [15]. A number of research works that correlate the effect of anisotropy on deep drawing can be found in Refs. [15–17]. However, when the orientation of materials is set to be random through H32 tempering [5], the effect coming from anisotropy might be omitted. Therefore, we focus more on the strain distribution as a result of deformation during the deep drawing process.

To date, most deep drawing processes have been performed at warm and elevated temperatures to avoid failures, whilst those operated in cold conditions (25 °C) are limited. In fact, improving the process temperature would increase the overall cost production [18,19]. Takuda et al. [18] documented that the ductility/formability of a 5182 Al alloy sheet improved notably with an increase in the working temperature to 250 °C utilizing a preheated die and blank sample at such a temperature, whilst the plunger was kept at a 25 °C temperature. Through this temperature gradient between the plunger, blank sample, and die, the optimized condition could be achieved. Unfortunately, the overall process utilizing the thermal gradient was time consuming and costly.

On the other hand, previous studies documented that warm (200–350 °C) deep drawing could increase the elongation and cup height of Al alloys series 5xxx and 6xxx up to 300% [19]. Kim et al. [19] suggested that the impact of forming temperatures on limiting drawing ratio (LDR) values was relatively insignificant under isothermal conditions. However, a noteworthy enhancement in formability was witnessed by maintaining the plunger at room temperature. Therefore, it can be deduced that by implementing a suitable temperature gradient on the workpiece, the formability of aluminum alloys can be improved. Comprehensive deformation traits were contrasted between constant temperature (isothermal) and varying temperature conditions (non-isothermal). Under isothermal condition, the plunger's corner area emerged as the critical failure site, where the limiting strain was observed to develop. In isothermal conditions, the critical failure location, where

the limit strain developed, was the plunger corner region. However, under conditions involving temperature gradients (non-isothermal), a comparatively uniform distribution of the strain and thinning was observed at the same depth within that particular section. This phenomenon indicated that the elevated temperature in the flange region delayed the onset of localized thinning and consequently shifted the point of failure towards the corner region of the die. This transition could be attributed to the improved ductility of the flange material and the increased flow stress within the plunger's corner region. A lower blank holder pressure (BHP) and friction coefficient were preferred to achieve an increased formability due to the decreased restraint force of the material.

Recently, Hou et al. [20] reported that deep drawing on the 7005 Al alloy at elevated temperature of 400~450 °C (in-die heating) improved the deep drawing performance of the alloy, which was manifested by the revolutionary change in sheet metal behavior—from the failure of deformation at lower temperatures (RT~200 °C) to achieving a limiting drawing ratio of 2.19 at 450 °C. In addition, the same study documented that the effect of temperature was recorded to contribute as high as ~63%, higher than the effect coming from the blank holder force (~26%) and drawing speed (~11%).

Therefore, we investigated the validity and reliability of the drawing process of Al alloy series 3xxx at room temperature. However, the efficiency and success of deep drawing can be further enhanced by harnessing the power of advanced analytical tools. A finite element (FE) analysis emerges as a critical tool in this context [21]. An FE analysis enables a proactive exploration of the deep drawing process before the metal even meets the press. By simulating the behavior of the material under different conditions and configurations, the FE method empowers manufacturers to predict optimal conditions, avert potential failures, and tailor the process for optimal outcomes [22]. Incorporating an FE analysis into the prelude of the deep drawing process offers a unique advantage: the ability to ascertain the most conducive conditions to the alloy's behavior. Key variables, such as the plunger radius and coefficient of friction, can be dissected and fine-tuned through virtual simulations, even before the first sheet is drawn. This predictive capacity does not only streamline the process but also reduces wastage, as unfavorable conditions can be spotted and rectified prior to production, improving cost-effectiveness, and increasing the production efficiency.

This paper focuses on a comprehensive exploration of the synergistic relationship between the Al alloy 3104-H32 and the preemptive potential of an FE analysis. By harnessing the predictive capabilities of the FE analysis, manufacturers can preemptively optimize conditions and prevent failure, ultimately contributing to the overall efficiency, cost-effectiveness, and success of the deep drawing process. Through a synthesis of theoretical insight, computational prowess, and practical implications, this study aims to shed light on the transformative impact of the FE analysis by considering the paramount importance of postdeformation strain distribution in the context of deep drawing practices.

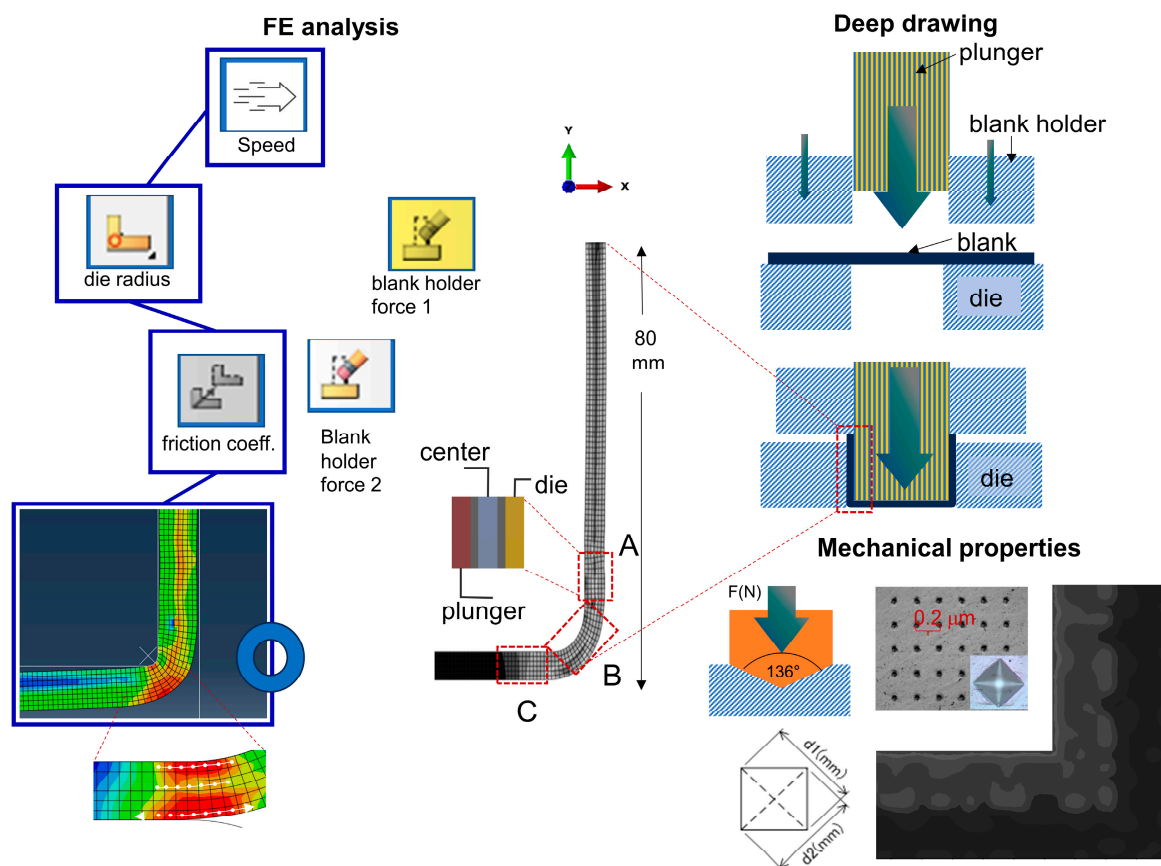
2. Materials and Methods

The present study focused on three aspects: (i) a simulation by the FE method, (ii) the deep drawing process to obtain a U-shaped Al container for a stack cell application, and (iii) a characterization. The FE analysis was carried out prior to the deep drawing process by utilizing five different scenarios involving the plunger radius and coefficient of friction parameters at a cold temperature (25 °C) and a fixed speed of 20 mm/s as listed in Table 1. MoS₂ was applied to the blank surface as the lubricant by a coating treatment and natural air drying that was applied at a rate of 27.0–33.0 gr/m². Two subsequent coatings were applied to increase the thickness of the lubricant. The material investigated in this study was a deep-drawn Al alloy series 3104-H32 with a chemical composition of 1.4 Mn, 1.3 Mg, 0.6 Si, 0.25 Cu, 0.25 Zn, and the balance of Al (in wt.%). The material was characterized by surface observation (Surfview 3D profiler), optical observation (OM, Olympus BX-51), and mechanical observation (Vickers microhardness, Wilson Instrument).

Table 1. Parameters of the finite element analysis.

| Parameters | C1 | C2 | C3 | C4 | C5 |
|--------------|------|------|------|-----|-----|
| Speed (mm/s) | 20 | 20 | 20 | 20 | 20 |
| Radius (mm) | 0 | 1.5 | 3.0 | 3.0 | 3.0 |
| Friction | 0.05 | 0.05 | 0.05 | 0 | 0.1 |

For the surface observation, the deep-drawn sample was cut from three different regions (as shown in Figure 1) with dimension of $30 \times 20 \times 2$ mm for each. The material surface interacting with the die (near-to-die) during the deep drawing process was the main surface to observe. In order to investigate the microstructure, the samples were ground, polished, and etched. Surfaces were mechanically ground using a #2400 grit SiC paper, followed by a mirror polishing until a 0.25 diamond suspension. Prior to immersion in the etching solution, polished surfaces were cleaned in an ultrasonic bath for 10 min. Poulant's reagent was used as the etching solution by mixing the 1st solution (1.25 mL of distilled water, 15 mL of HCl, 7.5 mL of HNO₃, and 1.25 mL of HF) and the 2nd solution (20 mL of chromic acid and 12.5 mL of HNO₃) together. The samples were analyzed along the z-axis (shown in the schematic illustration) and divided into three parts, near the plunger, the center, and near the die part. A microhardness test was conducted for further investigations.

**Figure 1.** Schematic to illustrate the simulation, deep drawing, and mechanical assessment of the current work.

3. Results

3.1. FEM Analysis

Equivalent Strain Distribution

Figure 2 shows an overview of the equivalent plastic strain (PEEQ) map generated from the Abaqus/Standard module for five different conditions, namely C1, C2, C3, C4, and C5. For C1 (Figure 2a) with a very small plunger radius (≈ 0), a severe strain (represented with the red color) was clearly detected at the outer surface near the die. At that particular position, two neighboring elements exhibited a severe local distortion with a PEEQ value larger than ~ 0.7 . Meanwhile, for parameter C2 (Figure 2b) with a plunger radius of 1.5, the distortion was alleviated (PEEQ in the range of 0.3~0.43) and distributed to a larger number of elements (in this case, nine neighboring elements). For condition C3, C4, and C5 (Figure 2c–e) with plunger radius of three at different friction coefficients, the distortion was further decreased to as low as 0.2. Up to there, the aforementioned condition seemed to exhibit similar characteristics.

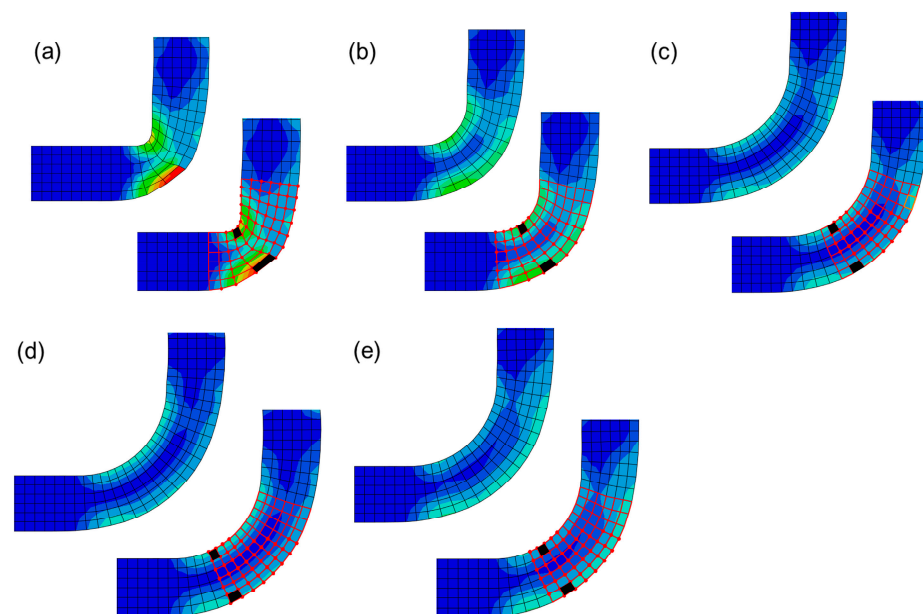


Figure 2. FEM results showing the strain distribution along the z-axis in five different combinations of two parameters: the plunger radius and the friction coefficient, (a) C1, (b) C2, (c) C3, (d) C4, and (e) C5. The highest level of homogeneity is shown by C5 in terms of stress distribution.

Figure 3 shows the distribution of the PEEQ value near the plunger, center, and die of the set elements highlighted with a red line in Figure 2. For C1 (Figure 3a), the PEEQ values severely fluctuated, and no uniform tendency was found near the plunger, center, and die. In Figure 3b, condition C2 with a plunger radius of 1.5 showed less fluctuations than C1, which suggested that the increase in plunger radius effectively decreased the amount of strain. However, the difference in term of effective strain near the plunger, center, and die were apparent. It is important to note that part near the plunger dominantly had the highest PEEQ values followed by the area near the die and then the center. When a plunger radius of three was used, the PEEQ values near the plunger and die were quite similar to each other. However, the PEEQ value at the center remained very low suggesting that the effective strain distribution was not uniformly distributed through the thickness of the workpiece. For condition C5 with a plunger radius of three and a friction of 0.1, despite the difference between the PEEQ values near the die and the plunger, the value at the center became closer, suggesting that additional straining occurred in the central part. A strain distributed throughout the thickness of the sample during deep drawing is important to avoid the formation of wrinkles [23]. Moreover, in C5, the PEEQ values of the region near the die was higher than that near the plunger, suggesting that C5 allowed the material

near to the die to flow more than that near the plunger. This is preferable since material positioned near the die should have more flow in order to avoid failure in the form of tears or a split [24].

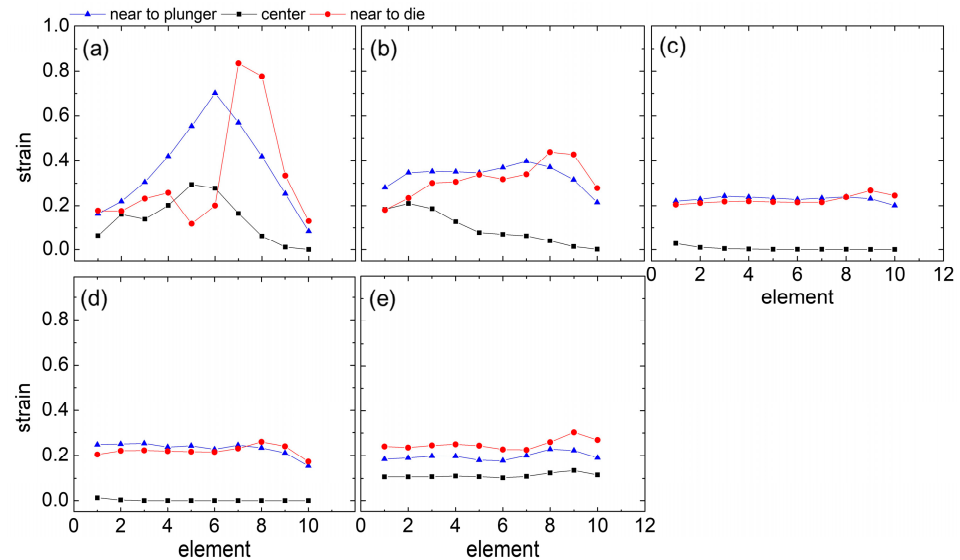


Figure 3. Curve showing the strain distribution of a local element taken from the corner of sample (a) C1, (b) C2, (c) C3, (d) C4, and (e) C5. These regions were subdivided in three different sections: near the plunger, center, and die portions.

Table 2 shows the strain of a specific element (highlighted with a black color in Figure 2) at two different times (2.1 and 2.4 s), the calculated strain rate, as well as the representative element geometry near the plunger and the die. Sample C1 and C2 showed a high strain rate (2.20 and 0.90 s^{-1}) but as shown previously in Figure 2, both effective strain distributions were nonuniform. Additionally, Table 2 displays how the representative elements were severely distorted, especially for C1 with the highest strain rate. For C2, with the improved stability in terms of strain distribution, the representative elements were not distorted as much as those of C1, C3, and C4, and C5 showed an even better strain distribution than that of C1 and C2. Here, the depth comparison was conducted between the three by considering the plastic strain components of PE11 and PE22 for normal strains, measuring the changes in length along x and y, respectively, together with PE12 for shear strains. It is noteworthy that these three conditions exhibited values of PE12 that were comparable to those of C2, suggesting that among the strain components, the shear strain was dominant. Shear strain, despite its complexity, is preferred to activate the slip system more in order to accommodate more deformation [25,26]. Among the three conditions with a radius of three, C5 showed an anomaly where all the strain components for the part near the plunger were smaller than in the other conditions, whereas most of the strain components for the part near the die were larger than those in the other conditions (the PE11 value for C5 was close to that for C3 and C4). This suggested that C5 allowed more accommodation of the deformation near the die of the corner which is known to be sensitive to developing defect [27–29]. Interestingly, among the conditions with a radius of three, C5 exhibited the highest strain rate (0.77 s^{-1}). This might explain the additional straining that occurred in the central part since an increase in strain rate resulted in increased strain [30].

Table 2. Strain, strain rate, and characteristic of an element near the plunger and near the die from the simulated conditions.

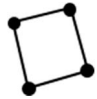
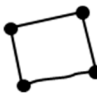
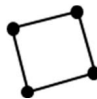
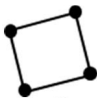

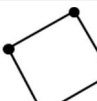
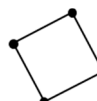
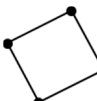
| | Time (s) | Strain ϵ | Strain Rate $\dot{\epsilon}$ (s^{-1}) | Near the Plunger Element | Near the Die Element |
|----|----------|-------------------|--|--|---|
| C1 | 2.1 | 0.096 | 2.20 |  |  |
| | 2.4 | 0.78 | | PE11 = -0.411 PE22 = -0.066 PE12 = -0.05 | PE11 = 0.358 PE22 = 0.076 PE12 = 1.187 |
| C2 | 2.1 | 0.041 | 0.90 |  |  |
| | 2.4 | 0.32 | | PE11 = -0.269 PE22 = -0.042 PE12 = -0.125 | PE11 = 0.093 PE22 = 0.057 PE12 = 0.482 |
| C3 | 2.2 | 0.001 | 0.70 |  |  |
| | 2.5 | 0.22 | | PE11 = -0.154 PE22 = -0.05 PE12 = -0.132 | PE11 = 0.041 PE22 = 0.06 PE12 = 0.329 |
| C4 | 2.2 | 0.003 | 0.70 |  |  |
| | 2.5 | 0.22 | | PE11 = -0.142 PE22 = -0.08 PE12 = -0.132 | PE11 = 0.041 PE22 = 0.065 PE12 = 0.333 |

Table 2. Cont.

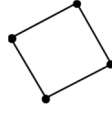
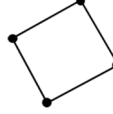
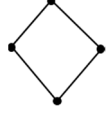

| | Time (s) | Strain ϵ | Strain Rate $\dot{\epsilon}$ (s^{-1}) | Near the Plunger Element | Near the Die Element |
|----|----------|-------------------|---|---|---|
| C5 | 2.2 | 0.0042 | 0.77 |  |  |
| | 2.5 | 0.245 | |  PE11 = -0.139 PE22 = -0.032 PE12 = -0.094 |  PE11 = 0.039 PE22 = 0.079 PE12 = 0.369 |

Figure 4 shows the d-drawn Al alloy for condition C5. It is clear that the result aligned well with the result predicted by the FE simulation. No failures were observed throughout the surface of the sample including the cornering region, which indicated a successful deep drawing process.

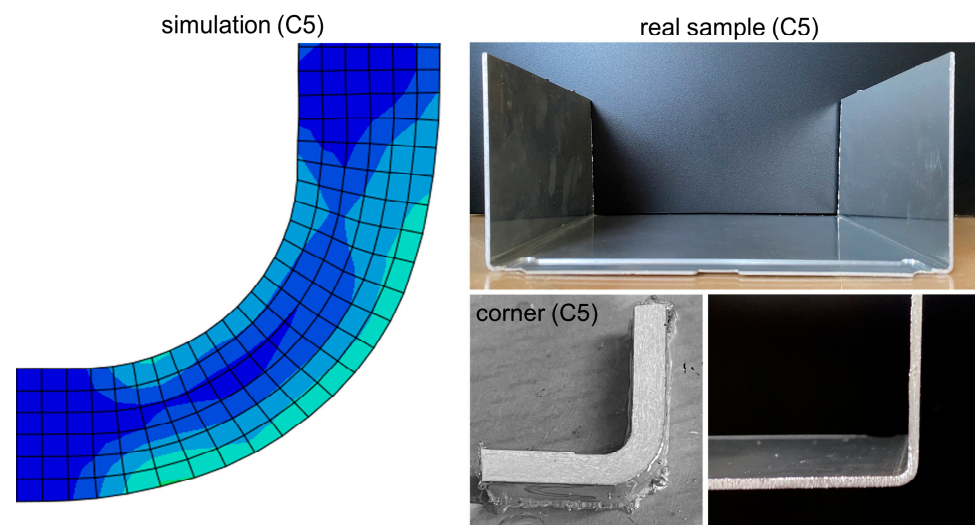


Figure 4. Simulation and experimental results of the optimized condition (C5) showing a good agreement.

3.2. Surface Morphologies

3.2.1. Surface Roughness

Figure 5 shows the surface roughness of the sample with the most optimized parameters (C5). The area of the sample was subdivided into regions A, B, and C. As shown in Figure 5a–c, the surface roughness was increased from the vertical region (A) to the corner (B), which suggested that the strain would be localized in the corner section. The results were parallel with the simulation data showing that the corner region B with the higher strain density (Figure 2e) would receive a larger deformation and induce a higher surface roughness. On the other hand, the roughness of region A and C near the corner showed almost the same value of $\sim 0.3 \mu\text{m}$, indicating that those regions received less strain compared to B. These results were in line with the simulation data shown in Figure 2e. Previous findings documented that a higher level of plastic deformation was received by the corner region, and as a consequence, such region would likely show a higher degree of surface

roughness [31–34]. This plastic deformation generated a localized strain concentration which further produced microscale irregularities and a roughness on the surface. These irregularities contributed to an increase in surface roughness.

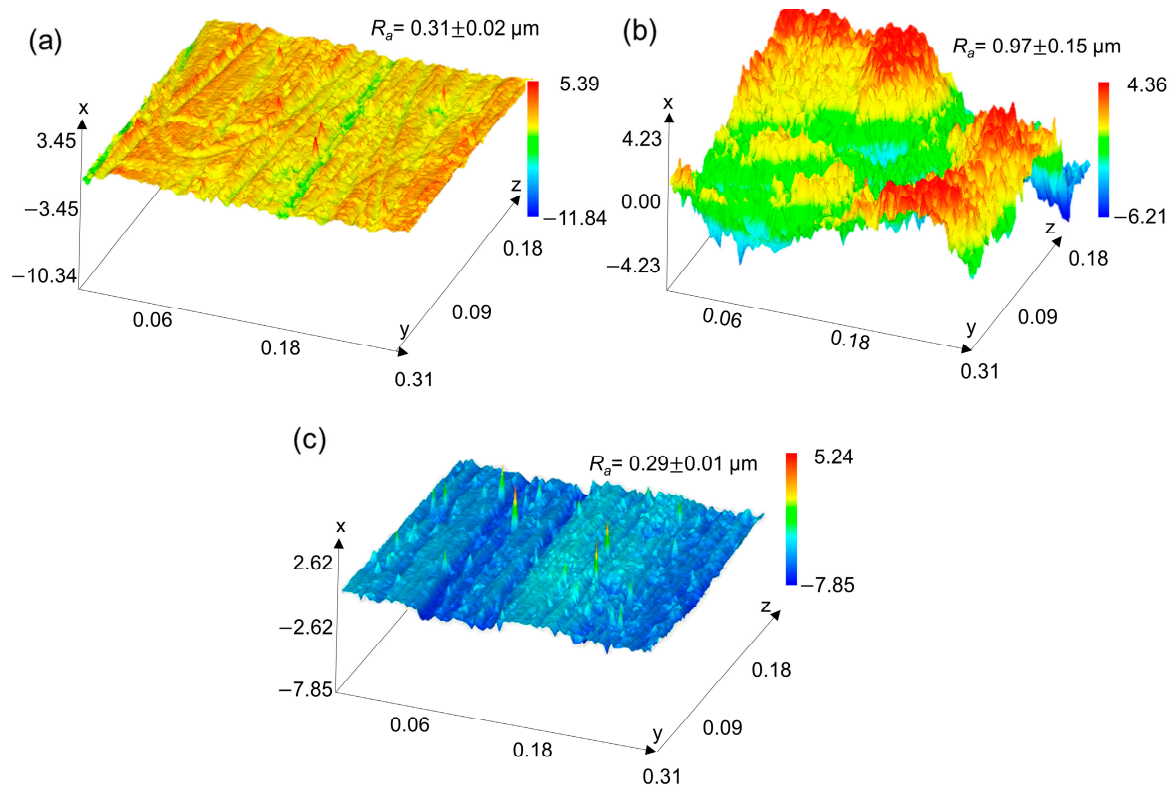


Figure 5. AFM images showing the surface roughness taken from the corner areas (a) A, (b) B, and (c) C. Area B (corner) showed the highest surface roughness, whilst areas A and C showed a lower surface roughness due to the low level of deformation.

3.2.2. Microstructures

Figure 6 shows the evolution of grain size of the FEM-optimized sample, C5, during the deep drawing process in three different regions of A, B, and C. Each region was divided into three different sections near the plunger, center, and die portions. In general, the region near the die showed a higher deformation effect, as can be seen from the elongated grain characteristics compared to the center and the region near the plunger. For B, the grains in the portion near the die exhibited an elongated grain as the lowest width among the other portions. This was in accordance with the result in Figure 2e where the elements located near the die portion exhibited the highest strain as shown by green and light blue colors. It is known that the grain width decreases with an increasing amount of strain [35]. Moreover, based on the results in Table 2, the shear strain component (PE12) near the die with $PE12 = 0.369$ was almost four times higher than that near the plunger with $PE12 = -0.094$. This finding supported the fine width of the elongated grains in the portion near the die [26]. The neighboring regions, A and C, exhibited a microstructure having a coarser width of elongated grains compared to B. Between the two regions, the elongated grains in C seemed to have a lower width than those in A. This was likely due to the different magnitude of the equivalent plastic strain where the amount of strain recorded near the C region was higher than that near the A region. This point is elaboratively discussed in the discussion section together with a figure with the recorded strain. It is believed that, although both A and C were located near B, the strain characteristics were likely to differ between the two regions.

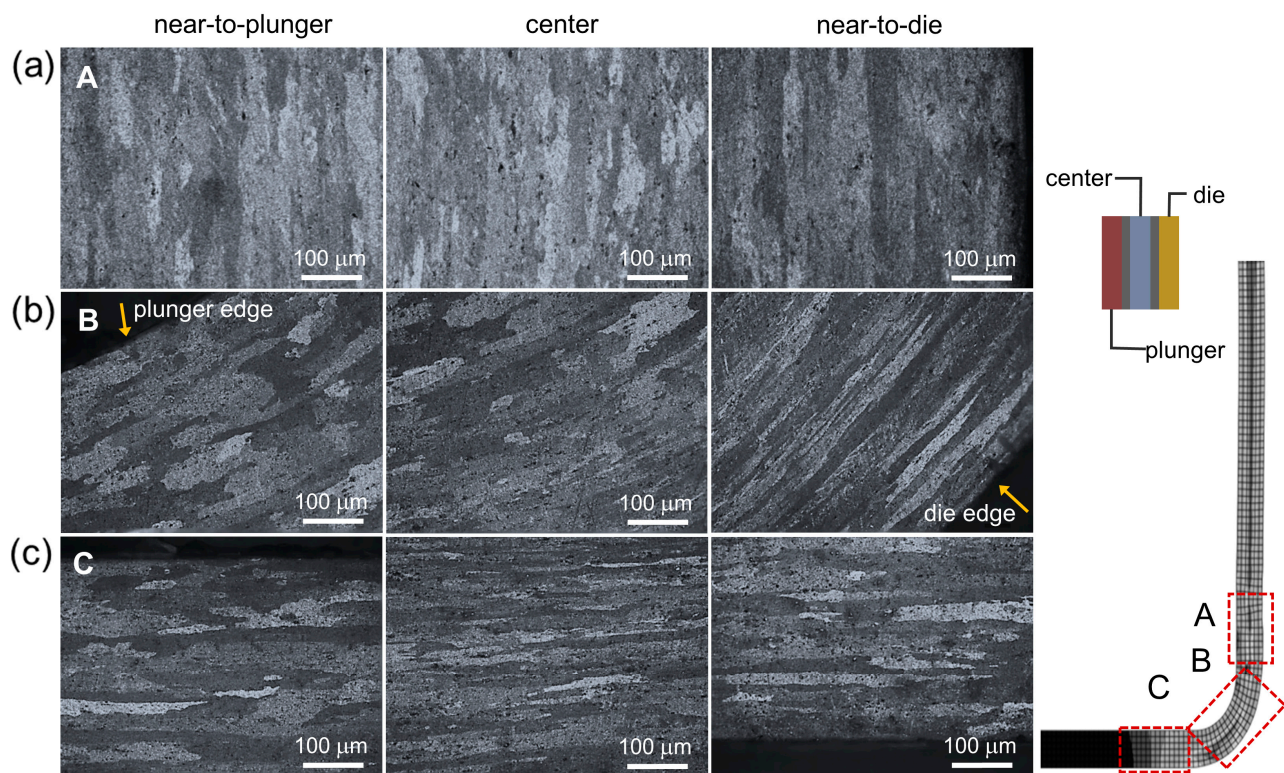


Figure 6. OM micrographs of the deep-drawn C5 sample taken from areas (a) A, (b) B, and (c) C. These regions were subdivided in three different sections: near the plunger, center, and die.

3.3. Mechanical Properties

Figure 7 shows the microhardness map obtained via a Vickers indentation of the optimized sample. The optimized sample exhibited a decent flow of material specifically at the part near the die, which resulted in an elongated grain as shown in Figure 6. The sample exhibited the highest hardness value at the part near the die and gradually decreased as it moved to the part near the plunger, which suggested the strengthening originated from the elongated grains near the die [36]. No significant discontinuity was seen in term of hardness value along the die part, which supported the result that the optimized condition was desirable for achieving a homogenous deformation at the corner of the sample. Although the resulting hardness analysis revealed an apparent difference in term of hardness between the parts near the plunger (~77 HV) and near the die (~84 HV), the hardness distribution near the plunger also exhibited a decent uniformity close to that near the die. It is important to mention that with the increase in hardness, the indentation mark showed a ductile behavior of the sample, suggesting that the strengthening was sufficiently good and prevented the materials from undergoing a fracture or surface failure.

The microhardness distribution of the optimized condition was likely in conjunction with the characteristics of the strain distribution where two localized strain distributions were located at the portions near the plunger and near the die, as shown in the simulation. In the case of C5, the strain experienced at its central region differed from that observed under other conditions. This likely triggered the formation of elongated but wider grains than those near the die portion. This might be associated with the existence of a strain with a dominant component of shear, which played a complex role in the microstructure as well as mechanical properties.

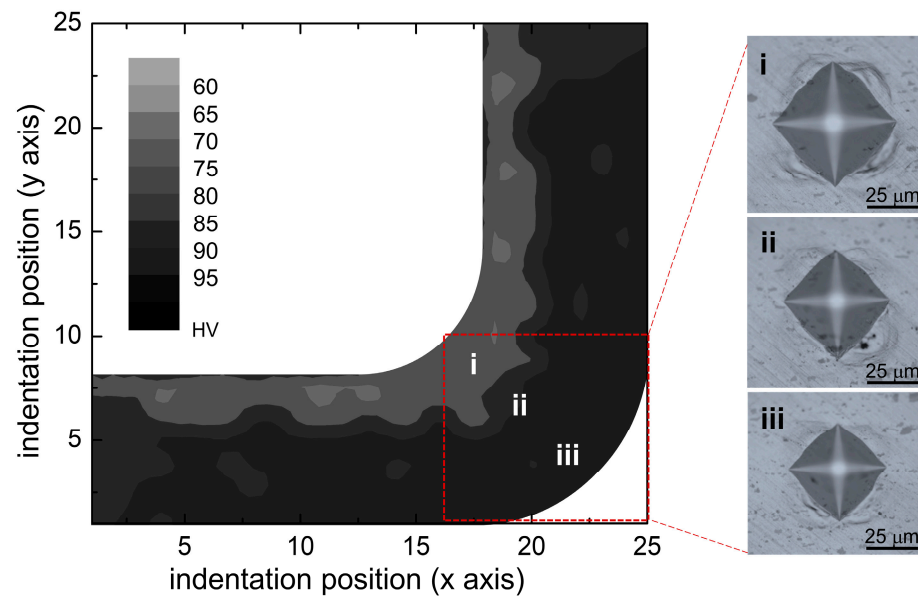


Figure 7. Microhardness maps of the sample taken from the corner of the optimized C5 sample. Three subdividing areas of microhardness were recorded in (i) near the plunger, (ii) center, and (iii) near the die.

4. Discussion

The successful deep drawing process by utilizing five different scenarios (C1~C5) implied the efficacy of the simulation method in predicting the materials' behavior and properties. Through the utilization of a finite element analysis, optimum parameters, namely, the plunger radius as well as the friction coefficient, were suggested. No cracks or failures were observed during the fabrication and test of the materials. Among the performed scenarios, C5 was found to be the optimum condition. An analysis considering both equivalent plastic strain at integration points (PEEQ) and plastic strain components at integration points (PE) were potentially useful to assess the flow tendency of material at different parts, together with the information about the active strain component.

Concerning the optimized condition, Figure 8 shows that C1, with a very low radius, had a localized strain distribution, which was in contrast with C5, with a radius of three, which had a uniform strain distribution. A distribution of PEEQ values for the highlighted element was shown. Starting from C, the PEEQ value was the highest and then decreased as it moved toward B and A. To explain the details, a series of meshes (six layers, 3432 elements) with an increasing step time was provided with the color representing the value of PEEQ (dark blue, blue, light blue, and green). The specific step times were chosen to show how the strain during deep drawing developed at the corner. A schematic illustration of the mechanism was proposed. At 0.100 s, the strain developed at two different spots located at the surfaces near the plunger and near the die surfaces (the two strains are termed as paired strains and represented by a blue color). As the plunger moved further downward (after 0.150 s), the paired strains expanded and tried to reach one another. Based on the simulation of several conditions, the rate for the expansion depends on the radius of the plunger, such that with a smaller radius, the rate of expansion would be higher, and the two strains would likely be unified. At 0.30 s, the two spots stopped expanding (in the case of C5, the paired strains did not unify) and started to propagate along the wall and variation values of the strain (represented by blue, light blue, and green) depending on the radius, such that a higher radius gave a stable value. The strain extended until it lined up in parallel with the radius. In other words, with a higher radius, the propagation takes longer.

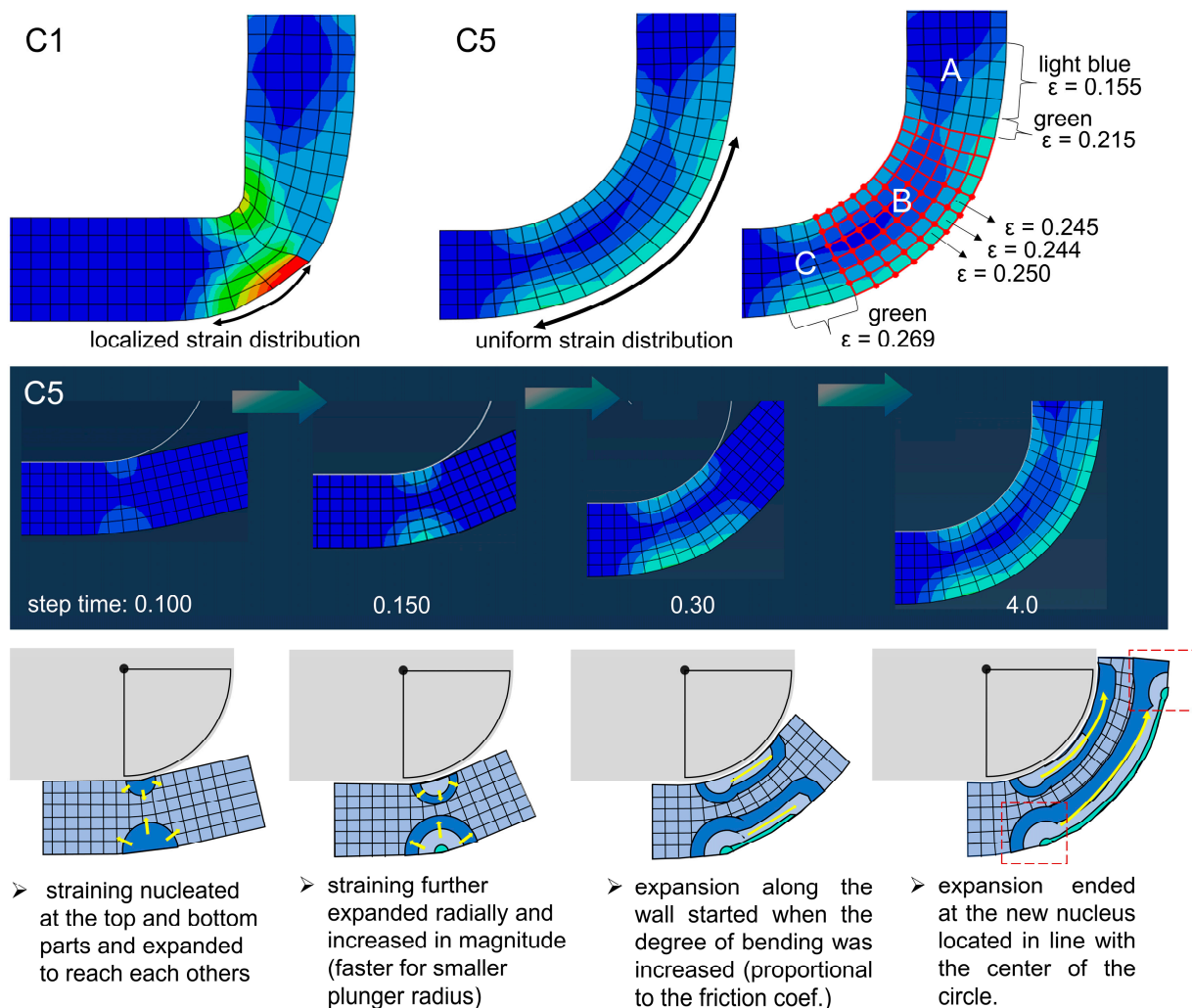


Figure 8. Schematic to illustrate the nucleation and propagation of strain for the optimized condition (C5).

Regarding the strain value near the plunger and the die, C5 exhibited a characteristic that was considered the best, such that the strain was larger near the die than near the plunger. This was believed to originate from the friction coefficient, as such a phenomenon occurred when the friction coefficient was increased from 0.05 to 0.1. It has been reported that a friction coefficient as small as possible is preferred, since it induces a homogeneous strain distribution [37]. It is also possible to increase the friction coefficient as long as no wrinkles are visible [38].

In the present study, although the strain was not uniformly distributed throughout the thickness during the first strain expansion, the straining characteristic in the C5 sample was such that the strain at the portion near the die was higher than that near the plunger, as shown by elongated green color. This is believed to be advantageous for the formability of metals under a deep drawing process. Lastly, based on the simulation, it can be seen that the strain pair finally unified after 4.0 s (this was not shown in the schematic). Such behavior is believed to originate from the relatively larger strain rate in C5 compared to C3 and C4. It has been reported that the strain increases with the increase in strain rate [30].

In this study, we suggested an optimum condition where during deep drawing, not only the deformation was imposed throughout the thickness, but such condition prioritized the accommodation of the deformation at the outer surface touching the die edge. This resulted in a smooth cornering as well as a uniform hardness distribution. It is likely that the friction coefficient played a significant role in triggering the aforementioned phenomenon.

This was in line with a previous report suggesting that friction imposed an indirect effect compared to a homogeneous deformation [19,39].

One of the main strain components that played a role here was shear strain, which not only helped to accommodate the deformation but also to generate an equiaxed substructure. In general, the accommodation via shear deformation occur in any interfacial area, without any preferences [40]. The optimized condition in this study allowed the shear deformation to occur at the outer surface touching the die edge, which was beneficial to minimize the chance of the formation of a surface defect.

The current result can be further improved if the orientation of each grain is taken into account, since a change in orientation will affect the flow behavior during plastic deformation [41]. In order to do that, a finite element analysis utilizing UMAT (User Materials) subroutine should be carried out to incorporate the orientation into the simulation so that even better prediction can be obtained.

5. Conclusions

We investigated the deformation of Al 3104-H32 sheet metals during a cold deep drawing process (25 °C) through the integration of experimental and finite element methods, which showed a good agreement between the two approaches. Among five different conditions, a nose plunger radius of 3 mm and a friction coefficient of 0.1 were considered as the optimum condition based on the bending characteristic. Such a condition was capable of inducing a lattice distortion and activate the slip system that was desired to accommodate more deformation. A strain history analysis revealed that the scenario allowed the elements located near the die surface to easily flow compared to those near the plunger, which was crucial to avoid failure in the form of tears or splits. The results on the mechanical properties revealed that the distribution of microhardness values was considerably improved, as shown by the value of the portions near the plunger (~77 HV) and near the die (~84 HV). A mechanism of strain development during bending was proposed, which could be used to precisely comprehend and forecast the strain distribution in a deep drawing process. Overall, our study contributes to the advancement of knowledge in this field and provides practical insights for optimizing sheet metal forming processes.

Author Contributions: Conceptualization, W.B., S.F., I.P.W., Y.G.K. and J.-H.K.; methodology, W.B., S.F., M.J.K. (Min Jun Kim), I.P.W. and Y.G.K.; software, W.B., D.-J.K. and M.J.K. (Myung Jae Kim); validation, W.B., S.F., I.P.W. and Y.G.K.; formal analysis, S.F., D.-J.K., M.J.K. (Myung Jae Kim), J.M.O. and J.-H.K.; investigation, W.B., S.F., J.H.G. and J.M.O.; resources, D.-J.K., M.J.K. (Min Jun Kim) and M.J.K. (Myung Jae Kim); data curation, J.H.G., M.J.K. (Min Jun Kim), D.-J.K. and J.M.O.; writing—original draft preparation, W.B. and S.F.; writing—review and editing, W.B., S.F., I.P.W., Y.G.K. and J.-H.K.; visualization, J.H.G., M.J.K. (Min Jun Kim), I.P.W. and Y.G.K.; supervision, D.-J.K., I.P.W. and Y.G.K.; project administration, Y.G.K.; funding acquisition, Y.G.K. All authors have read and agreed to the published version of the manuscript.

Funding: This work was supported by Industry-University-Institute Joint R&D Project in conjunction with SeA Mechanics Co., Ltd. funded by the Korea Industrial Complex Corporation (#222C000894) and supported partly by Industrial Innovation Talent Growth Project of the Korean Ministry of Trade, Industry and Energy funded by Korea Institute for Advancement of Technology (#P0023676, Expert Program for Sustainable Metals Industry).

Data Availability Statement: The data presented in this study are contained within the article.

Conflicts of Interest: The authors declare no conflict of interest.

References

1. Schneider, R.; Grant, R.J.; Schlosser, J.M.; Rimkus, W.; Radlmayr, K.; Grabner, F.; Maier, C. An Investigation of the Deep Drawing Behavior of Automotive Aluminum Alloys at Very Low Temperatures. *Metall. Mater. Trans. A Phys. Metall. Mater. Sci.* **2020**, *51*, 1123–1133. [[CrossRef](#)]
2. Ramulu, P.J. *Aluminum Alloys Behavior during Forming*; IntechOpen: London, UK, 2019; ISBN 978-1-78984-514-3.

3. Benedyk, J.C. International Temper Designation Systems for Wrought Aluminum Alloys: Part I—Strain Hardenable (H Temper) Aluminum Alloys. *Light Met. Age* **2009**, *67*, 26–30.
4. Aamir, M.; Giasin, K.; Tolouei-Rad, M.; Vafadar, A. A Review: Drilling Performance and Hole Quality of Aluminium Alloys for Aerospace Applications. *J. Mater. Res. Technol.* **2020**, *9*, 12484–12500. [[CrossRef](#)]
5. Ahmed, M.M.Z.; El-Sayed Seleman, M.M.; Sobih, A.M.E.S.; Bakkar, A.; Albaijan, I.; Touileb, K.; Abd El-Aty, A. Friction Stir-Spot Welding of AA5052-H32 Alloy Sheets: Effects of Dwell Time on Mechanical Properties and Microstructural Evolution. *Materials* **2023**, *16*, 2818. [[CrossRef](#)] [[PubMed](#)]
6. Vollertsen, F.; Hu, Z.; Niehoff, H.S.; Theiler, C. State of the Art in Micro Forming and Investigations into Micro Deep Drawing. *J. Mater. Process. Technol.* **2004**, *151*, 70–79. [[CrossRef](#)]
7. Hattalli, V.L.; Srivatsa, S.R. Sheet Metal Forming Processes—Recent Technological Advances. *Mater. Today Proc.* **2018**, *5*, 2564–2574. [[CrossRef](#)]
8. Dalong, L.; Yanting, L.; Enlin, Y.; Yi, H.; Feng, L. Theoretical and Experimental Study of the Drawing Force under a Current Pulse. *Int. J. Adv. Manuf. Technol.* **2018**, *97*, 1047–1051. [[CrossRef](#)]
9. Becker, N.; Pöhlndt, K.; Lange, K. Improvement of the Plane-Strain Compression Test for Determining Flow Curves. *CIRP Ann.-Manuf. Technol.* **1989**, *38*, 227–230. [[CrossRef](#)]
10. Singh, D.; Yousefi, R.; Boroushaki, M. Identification of Optimum Parameters of Deep Drawing of a Cylindrical Workpiece Using Neural Network and Genetic Algorithm. *World Acad. Sci. Eng. Technol.* **2011**, *78*, 211–217.
11. Colgan, M.; Monaghan, J. Deep Drawing Process: Analysis and Experiment. *J. Mater. Process. Technol.* **2003**, *132*, 35–41. [[CrossRef](#)]
12. Yusop, N.M.; Abdullah, A.B. Evaluation of Square Deep Drawn AA6061-T6 Blank Based on Thinning Pattern. *IOP Conf. Ser. Mater. Sci. Eng.* **2019**, *670*, 8–14. [[CrossRef](#)]
13. Horton, P.M.; Allwood, J.M.; Cleaver, C.; Nagy-Sochacki, A. An Experimental Analysis of the Relationship between the Corner, Die and Punch Radii in Forming Isolated Flanged Shrink Corners from Al 5251. *J. Mater. Process. Technol.* **2020**, *278*, 116486. [[CrossRef](#)]
14. Padmanabhan, R.; Oliveira, M.C.; Alves, J.L.; Menezes, L.F. Influence of Process Parameters on the Deep Drawing of Stainless Steel. *Finite Elem. Anal. Des.* **2007**, *43*, 1062–1067. [[CrossRef](#)]
15. Liu, W.; Huang, J.; Pang, Y.; Zhu, K.; Li, S.; Ma, J. Multi-Scale Modelling of Evolving Plastic Anisotropy during Al-Alloy Sheet Forming. *Int. J. Mech. Sci.* **2023**, *247*, 108168. [[CrossRef](#)]
16. Shahzamanian, M.M.; Wu, P.D. Study of Forming Limit Diagram (FLD) Prediction of Anisotropic Sheet Metals Using Gurson Model in M-K Method. *Int. J. Mater. Form.* **2021**, *14*, 1031–1041. [[CrossRef](#)]
17. Shahzamanian, M.M. Anisotropic Gurson-Tvergaard-Needleman Plasticity and Damage Model for Finite Element Analysis of Elastic-Plastic Problems. *Int. J. Numer. Methods Eng.* **2018**, *115*, 1527–1551. [[CrossRef](#)]
18. Takuda, H.; Mori, K.; Masuda, I.; Abe, Y.; Matsuo, M. Finite Element Simulation of Warm Deep Drawing of Aluminium Alloy Sheet When Accounting for Heat Conduction. *J. Mater. Process. Technol.* **2002**, *120*, 412–418. [[CrossRef](#)]
19. Kim, H.S.; Koç, M.; Ni, J. Development of an Analytical Model for Warm Deep Drawing of Aluminum Alloys. *J. Mater. Process. Technol.* **2008**, *197*, 393–407. [[CrossRef](#)]
20. Hou, J.; Deng, P.; Wang, S.; Xu, H.; Shi, Y. Study on Formability and Microstructure Evolution of Hot Deep Drawing Manufactured 7005 Aluminum Alloy Sheet Metal. *Mater. Today Commun.* **2023**, *36*, 106794. [[CrossRef](#)]
21. Szlosarek, R.; Holzmüller, P.; Kröger, M. Analyzing the Fretting Fatigue of Bolt Joints by Experiments and Finite Element Analysis. *Lubricants* **2023**, *11*, 348. [[CrossRef](#)]
22. Barrett, T.J.; Knezevic, M. Deep Drawing Simulations Using the Finite Element Method Embedding a Multi-Level Crystal Plasticity Constitutive Law: Experimental Verification and Sensitivity Analysis. *Comput. Methods Appl. Mech. Eng.* **2019**, *354*, 245–270. [[CrossRef](#)]
23. Nesterova, E.V.; Bacroix, B.; Teodosiu, C. Microstructure and Texture Evolution under Strain-Path Changes in Low-Carbon Interstitial-Free Steel. *Metall. Mater. Trans. A Phys. Metall. Mater. Sci.* **2001**, *32*, 2527–2538. [[CrossRef](#)]
24. Raju, S.; Ganesan, G.; Karthikeyan, R. Influence of Variables in Deep Drawing of AA 6061 Sheet. *Trans. Nonferrous Met. Soc. China* **2010**, *20*, 1856–1862. [[CrossRef](#)]
25. Kishor, N.; Ravi Kumar, D. Optimization of Initial Blank Shape to Minimize Earing in Deep Drawing Using Finite Element Method. *J. Mater. Process. Technol.* **2002**, *130–131*, 20–30. [[CrossRef](#)]
26. Edwards, T.E.J.; Di Gioacchino, F.; Goodfellow, A.J.; Mohanty, G.; Wehrs, J.; Michler, J.; Clegg, W.J. Transverse Deformation of a Lamellar TiAl Alloy at High Temperature by in Situ Microcompression. *Acta Mater.* **2019**, *166*, 85–99. [[CrossRef](#)]
27. Ikumapayi, O.M.; Afolalu, S.A.; Kayode, J.F.; Kazeem, R.A.; Akande, S. A Concise Overview of Deep Drawing in the Metal Forming Operation. *Mater. Today Proc.* **2022**, *62*, 3233–3238. [[CrossRef](#)]
28. Fan, J.P.; Tang, C.Y.; Tsui, C.P.; Chan, L.C.; Lee, T.C. 3D Finite Element Simulation of Deep Drawing with Damage Development. *Int. J. Mach. Tools Manuf.* **2006**, *46*, 1035–1044. [[CrossRef](#)]
29. Zareh-Desari, B.; Davoodi, B.; Vedaei-Sabegh, A. Investigation of Deep Drawing Concept of Multi-Point Forming Process in Terms of Prevalent Defects. *Int. J. Mater. Form.* **2017**, *10*, 193–203. [[CrossRef](#)]
30. Reddy, A.C. Formability of High Temperature and High Strain Rate Superplastic Deep Drawing Process for AA2219 Cylindrical Cups. *Int. J. Adv. Res.* **2015**, *10*, 1016–1024.

31. Nie, N.; Su, L.; Deng, G.; Li, H.; Yu, H.; Tieu, A.K. A Review on Plastic Deformation Induced Surface/Interface Roughening of Sheet Metallic Materials. *J. Mater. Res. Technol.* **2021**, *15*, 6574–6607. [[CrossRef](#)]
32. Furushima, T.; Tsunozaki, H.; Hirose, Y. Fracture and Surface Roughening Behaviors in Micro Metal Forming. *Procedia Manuf.* **2018**, *15*, 1481–1486. [[CrossRef](#)]
33. Tiwari, A.; Almqvist, A.; Persson, B.N.J. Plastic Deformation of Rough Metallic Surfaces. *Tribol. Lett.* **2020**, *68*, 129. [[CrossRef](#)]
34. Basak, S.; Prasad, K.S.; Sidpara, A.M.; Panda, S.K. Single Point Incremental Forming of AA6061 Thin Sheet: Calibration of Ductile Fracture Models Incorporating Anisotropy and Post Forming Analyses. *Int. J. Mater. Form.* **2019**, *12*, 623–642. [[CrossRef](#)]
35. Loorent, Z.; Ko, Y.G. Effect of Differential Speed Rolling Strain on Microstructure and Mechanical Properties of Nanostructured 5052 Al Alloy. *J. Alloys Compd.* **2014**, *586*, S205–S209. [[CrossRef](#)]
36. Bozcheloei, J.E.; Sedighi, M.; Hashemi, R. The Effect of Temperature on the Mechanical Properties and Forming Limit Diagram of Al 5083 Produced by Equal Channel Angular Rolling. *Int. J. Adv. Manuf. Technol.* **2019**, *105*, 4389–4400. [[CrossRef](#)]
37. Yang, T.S. Investigation of the Strain Distribution with Lubrication during the Deep Drawing Process. *Tribol. Int.* **2010**, *43*, 1104–1112. [[CrossRef](#)]
38. Tiwari, P.R.; Rathore, A.; Bodkhe, M.G. Factors Affecting the Deep Drawing Process—A Review. *Mater. Today Proc.* **2022**, *56*, 2902–2908. [[CrossRef](#)]
39. Roizard, X.; Pothier, J.M.; Hihn, J.Y.; Monteil, G. Experimental Device for Tribological Measurement Aspects in Deep Drawing Process. *J. Mater. Process. Technol.* **2009**, *209*, 1220–1230. [[CrossRef](#)]
40. Efe, M.; Gwalani, B.; Tao, J.; Song, M.; Kaspar, T.C.; Devaraj, A.; Rohatgi, A. Nanomechanical Scratching Induced Local Shear Deformation and Microstructural Evolution in Single Crystal Copper. *Appl. Surf. Sci.* **2021**, *562*, 150132. [[CrossRef](#)]
41. Chen, J.; Wei, H.; Zhang, X.; Peng, Y.; Kong, J.; Wang, K. Flow Behavior and Microstructure Evolution during Dynamic Deformation of 316 L Stainless Steel Fabricated by Wire and Arc Additive Manufacturing. *Mater. Des.* **2021**, *198*, 109325. [[CrossRef](#)]

Disclaimer/Publisher's Note: The statements, opinions and data contained in all publications are solely those of the individual author(s) and contributor(s) and not of MDPI and/or the editor(s). MDPI and/or the editor(s) disclaim responsibility for any injury to people or property resulting from any ideas, methods, instructions or products referred to in the content.